Arabian Journal of Chemistry (2023) 16, 105157

King Saud University

Arabian Journal of Chemistry

www.ksu.edu.sa
www.sciencedirect.com

ORIGINAL ARTICLE

Flower-like CoP coated $NiMoO_4$ nanorods as self-supported core-shell heterojunction electrode can facilitate oxygen evolution reaction at a low overpotential

Nu Wang [a], **Kai Huo** [a], **Hongli Zhu** [b], **Haoran Zi** [c], **Yan Shan** [a,*], **Kezheng Chen** [a], **Xuegang Yu** [a,*]

[a] *Lab of Functional and Biomedical Nanomaterials, College of Materials Science and Engineering, Qingdao University of Science and Technology, Qingdao 266042, China*
[b] *Institute 53 of China's Ordnance Industry, Jinan 250031, China*
[c] *Chinese People's Liberation Army 32382 Unit, Beijing, 100072, China*

Received 9 May 2023; accepted 8 July 2023
Available online 11 July 2023

KEYWORDS

$NiMoO_4$ nanorods arrays;
CoP nanosheets;
Self-supported core-shell structure;
Heterojunction;
Oxygen evolution reaction;
DFT

Abstract Transition metal phosphates, as the most promising catalyst for oxygen evolution reaction (OER), have attracted much attention in recent years. In this work, CoP nanosheets are electrodeposited on $NiMoO_4$ nanorods to form a self-supported core-shell structure electrode with CoP-$NiMoO_4$ heterojunctions. Density functional theory (DFT) calculations demonstrate CoP-12@$NiMoO_4$/NF electrode can reduce reaction energy barrier of rate-determining step (RDS) from 8.743 eV to 2.519 eV. In 1 M KOH, the electrode shows a low overpotential of 165 mV (10 mA cm^{-2}), a low Tafel slope of 45 mV dec^{-1} and the significant stability. Compared with other non-noble metal OER electrocatalysts, the prepared CoP-12@$NiMoO_4$/NF electrode exhibits better electrocatalytic activity, which can provide a new choice of electrocatalysts for future practical applications.

1. Introduction

With the rapid increase of population around the world, the traditional fossil fuel is promptly exhausted, and the development of renewable energy is urgent. Nowadays, H_2 has attracted extensive attention attributed to the high energy density (~142 MJ kg^{-1}) and the water obtained after combustion, which is zero-carbon emission and a range of renewable energy sources, such as hydro and solar, as well as wind can provide electricity for producing H2 (Turner, 2004; Chu and Majumdar, 2012; Jin et al., 2021; Yu et al., 2019). By converting the

---

* Corresponding authors.
E-mail addresses: shanyan@qust.edu.cn (Y. Shan), yuxuegang@qust.edu.cn (X. Yu).

Peer review under responsibility of King Saud University.

ELSEVIER Production and hosting by Elsevier

https://doi.org/10.1016/j.arabjc.2023.105157
1878-5352

surplus electric energy into chemical energy of H_2, the energy crisis will be greatly alleviated. Of all the ways of producing H_2, electrolysis of water is not only a mature and simple technology, but also it is the most sustainable and promising route, which could be used widely in the future.

Generally, a complete electrolysis of water system is composed of corresponding half reaction on two electrodes: one is hydrogen evolution reaction (HER), which is a process for transferring of two electrons and the other is oxygen evolution reaction (OER), which is a process for transferring of four electrons (Li et al., 2021; Wu et al., 2022). They react at the cathode and anode, respectively. The huge overpotential for electrolysis of water is attributed to the need for enough energy to form a rigid O-O double bond (Dastafkan et al., 2019) with a process of complex multiple proton coupling and electron transfer (Shen et al., 2022; Yu et al., 2018). At present, the catalysts used for electrolysis of water mainly rely on precious metals (such as RuO_2, IrO_2) to reduce overpotential, but the disadvantages of scarcity, high cost and single function have seriously hindered the commercialization of the electrolysis of water (Wang et al., 2021; Wu et al., 2021; Yu et al., 2017). Therefore, the OER catalysts of metal hydroxides (Wang et al., 2021), sulfides (Yoon and Kim, 2016) carbides (Yu et al., 2020) selenides (Zhang et al., 2022) have attracted inclusive attention because of their abundant resources and higher catalytic performance. However, they are still not satisfactory enough due to the relatively poor intrinsic conductivity and limited exposure catalytic sites (Li et al., 2020). In general, the main intrinsical reason for the low efficiency is usually attributed to the slow rate of electron transfer in the catalyst. OER, as we know, is a reaction occurring on the surface, therefore, the microstructure of catalyst plays a significant role in the interaction between electrode and electrolyte. So abundant active area and fast charge transfer are achieved to increase the OER performance by adjusting the morphology and heterojunction structure. For this reason, we have developed catalyst directly on 3D structure to form a self-supported core-shell structure electrode with heterojunction, which can increase specific surface area, minimize agglomeration and accelerate charge transfer. Meanwhile the synergies between core-shell components are also beneficial to promote OER performance.

Recently, NiMo-based catalysts (such as MoNi4 (Zhang et al., 2017), NiMoO4 (Zhang et al., 2020), NiMoN (Wang et al., 2018) have been widely researched mainly due to the excellent water decomposition ability of Ni atoms. Among this series high performance OER catalysts, $NiMoO_4$ with unique nanorod arrays, abundant active site and simple synthesis route is used as the core component for OER (Chen et al., 2018). $NiMoO_4$, binary metal oxides, two metal cations interact with each other, which could lead to higher oxidation states, result in metal atoms more likely to bond with oxygen atoms to enhance electrochemical performance. However, in core-shell structures, shell components are always composed of oxides, so it is necessary to explore other materials. Transition metal phosphides (TMPs) have shown excellent HER activity when combined with the most abundant metallic elements on earth, but there are few studies and reports on the OER performance of TMPs so far (Xiao et al., 2015). Therefore, cobalt phosphide (CoP) was selected as the research object for OER in this work. Metal phosphorus has lone pair electrons in 3p and free 3d orbitals, which can accelerate electron transfer and promote OER performance (Yan et al., 2015). In the core-shell structure, composite nanostructures usually show better catalytic performance due to the synergistic ability between different components (Yan et al., 2010). So we used the method of electrodeposition to compound CoP and $NiMoO_4$ to achieve high efficiency of OER. Some studies on transition metal phosphides of OER have also been reported. Chen et al. doped the original Co_3O_4 which is after simple acidification with P atoms, showing a high P atoms doping amount as high as 6.1 wt%, forming the lattice distortion and rich structural defects, significantly reducing the overpotential (276 mV), which strongly enhanced the OER performance (Chen et al., 2022). Kim et al. studied the OER performance of Ni-Cu-P prepared by direct electrodeposition, and proved that phosphorus attracted some positive charges during OER and led them closer to the active metal center so that the overpotential was only 307 mV, which greatly enhanced the OER reactivity (Kim et al., 2018). However, the OER activity of TMPs is still not satisfying enough, therefore many strategies to improve the OER performance have been used at present, such as defect engineering (Dutta et al., 2016), doping (Ma et al., 2017); regulating morphology (Bhanja et al., 2020). In general, there are two main routes to enhance the OER activity: (i) subjoin the amount of active sites and the ability to contact with the electrolyte. (ii) accelerate electron transfer during OER and promote the release of the generated oxygen (Yang et al., 2019; Ghosh and Basu, 2018).

Herein, we have prepared CoP-12@$NiMoO_4$/NF electrode with self-supported core-shell heterojunction, which was a highly efficient electrode for OER. In the core-shell structure, a large area of sheet to sheet microstructure was formed, which was conducive to the reaction between electrode and electrolyte due to abundant active sites. The electrode showed a small overpotential (165 mV@ 10 mA cm^{-2}) in 1 M KOH as well as a low Tafel slope of 45 mV dec^{-1} and excellent durability. The current density of 25 mA cm^{-2} can maintain OER stability after 10 h. This work provided an innovative method for reasonably designing low cost, high performance and good electrochemical energy conversion.

2. Experimental section

2.1. Chemicals and reagents

The $Co(NO_3)_2 \cdot 6H_2O$ ($\geq$98.5%), ammonium fluoride (NH_4F, $\geq$96%), ammonium molybdate ($(NH_4)_6Mo_7O_{24} \cdot 4H_2O$, $\geq$98%), potassium hydroxide (KOH, $\geq$85%) and ethanol (C_2H_5OH) were obtained from Sinopharm Co., Ltd. Sodium hypophosphite ($NaH_2PO_2 \cdot H_2O$, $\geq$99%) was obtained from Tianjin Beilian Fine Chemicals Development Co., Ltd. Nickel sulfate hexahydrate ($NiSO_4 \cdot 6H_2O$, $\geq$98.5%) was obtained from Tianjin Zhiyuan Chemical Reagent Co., Ltd. All reagents and chemicals were used without further purification.

2.2. The preparation of $NiMoO_4$/NF

Normally, a piece of commercial nickel foam (1 × 5 cm^2) was washed for 10 min under ultrasonic waves with 3 M HCl solution, deionized water (DI) and ethanol in turn. This step of pretreatment could remove nickel oxide, oil and various organic pollutants from the surface of nickel foam. Then NF was dried naturally at room temperature. After that, dissolved 8 mmol $NiSO_4 \cdot 6H_2O$ (2.103 g) and 2 mmol $(NH4)_6Mo_7O_{24} \cdot 4H_2O$ (2.472 g) in 50 ml of DI water and mixed the solution continuously until a clear and transparent solution was formed, then transferred the solution into an 80 ml teflon-lined autoclave and put the washed NF in it. The autoclave was heated at 150 °C for 6 h after sealing. Until the system was at room temperature, the NF with yellow–brown sediment was rinsed repeatedly with DI water and ethanol. Afterwards, the sample was dried in an oven at 60 °C overnight.

2.3. The formation of CoP@$NiMoO_4$/NF with electrodeposition

The CoP@$NiMoO_4$/NF was prepared by electrodeposition. The solution of electrodeposition was constituted of 20 mmol $Co(NO_3)_2 \cdot 6H_2O$ (5.82 g), 20 mmol $NaH_2PO_2 \cdot H_2O$ (2.12 g), 25 mmol NH_4F (0.925 g) and 50 ml DI water. The $NiMoO_4$/NF electrode and carbon rod played a role in the working and counter electrodes, respectively. Electrodeposition of CoP was prepared at a constant current density of 100 mA cm^{-2}. The samples were recorded as CoP-X@$NiMoO_4$/NF by changing the deposition time (X = 1, 6, 9, 12, 15 min). The obtained samples were washed with DI water and ethanol several times, and dried overnight in an oven at 60 °C. The mass loading of the CoP-12@$NiMoO_4$ was 0.5 mg cm^{-2}. And other relevant information was in Supporting Information.

3. Results and discussion

3.1. Materials synthesis and characterization

Scheme 1 illustrated the preparation of self-supported CoP-12@$NiMoO_4$/NF electrode with core-shell heterojunction structures. Nickel foam (NF) with low cost and excellent conductivity was used as the base. $NiMoO_4$ nanorod arrays had grew successfully on the surface of NF under a hydrothermal route. Next, CoP nanosheets were prepared by electrodeposition on $NiMoO_4$ nanorod arrays. The color of NF changed from light silver to dark yellow and then to light blue during the above preparation process, indicating that the various products had been prepared successfully.

The image in Fig. 1a showed that a large number of $NiMoO_4$ nonorod arrays with smooth surfaces grew uniformly on the surface of NF. The self-supported $NiMoO_4$ nanorod arrays could expose more active sites and also facilitate mass diffusion to further improve the catalytic activity under a high current density. The images in Fig. 1b and Fig. S1a showed that the flower-like CoP nanosheets had been electrodeposited successfully on NF. Plentiful lamellar structures were conducive to the formation of active sites and the enhancement of electron transport. As the images in Fig. 1c and Fig. S1b shown, it was observed that abundant CoP nanosheets grew on the surface of $NiMoO_4$ nanorod arrays, which strongly demonstrated that CoP-12@$NiMoO_4$/NF was core-shell structure, with $NiMoO_4$ nanorods acting as the core and CoP nanosheets as the shell. CoP nanosheets with crumpled morphology were observed on the gaps between rods and laminas, confirming that $NiMoO_4$ nanorods were bridged and entangled by CoP nanosheets. In such a structure, CoP nanosheets could act as a conductive network of shuttled electrons. It was worth noting that the prepared unique core-shell structure had plentiful rough surfaces, which contributed to the oxygen adsorption, thus promoting the reaction with electrolyte. Also, the adequate interlamellar space provided a release channel for the generated oxygen, consequently enhancing the stability of OER under a high current density (Liu et al., 2020). TEM analysis further confirmed the SEM results. Fig. 1d showed the prepared $NiMoO_4$ nanorods with obvious lattice distance of 0.668 nm, which correspond to PDF#12–0348. From Fig. S2a, the lattice distances of $NiMoO_4$ phase was 0.336 nm, which correspond to PDF#45–0142. These two phases were both proved by XRD. And in Fig. 1e, it was found that CoP nanosheets grew densely on $NiMoO_4$ nanorods to form the core-shell structure, which were exactly shown as the SEM image. As shown in Fig. 1f, there obviously existed heterojunction interface between $NiMoO_4$ phase and CoP phase. It demonstrated the lattice spacing of 0.335 nm and 0.371 nm, which correspond to $NiMoO_4$(2 2 0) and CoP (1 0 1) lattice plane respectively. Fig. 1g was the HRTEM image of CoP nanosheets, in which amorphous substances could be observed in the red region. Furthermore, the crystal lattice was clearly found with the planes spacing of 0.244 nm, which was consistent with (1 0 2) planes of CoP (PDF#29–0497). Obviously, CoP contained both crystalline and amorphous substances, where the boundary between the crystalline substances and the amorphous substances provided more active sites of Co^{3+} to accelerate the OER process. The formation of amorphous phosphates was very favorable for producing large active regions and active sites which were deeply exposed (Guo et al., 2018). The amorphous structure of high energy state can give low activation energy of electron transfer on the surface, because the long-range disordered structure lowered the energy barrier, so that it can significantly improve the catalytic activity. The distribution of Ni, Co, O, Mo and P elements were confirmed in the EDX mapping of Fig. 1h. From Fig. 1h, it can be seen obviously that Ni, Mo and O were mainly distributed on nanorods, while Co and P were mainly distributed on nanosheets, which indicated that CoP-12@$NiMoO_4$/NF had been successfully prepared.

The crystal structure and composition of the products at different stages were analyzed by XRD. The powders for XRD characterization were obtained from the surface of NF. As shown in Fig. 2a, the diffraction peaks at 9.83°,

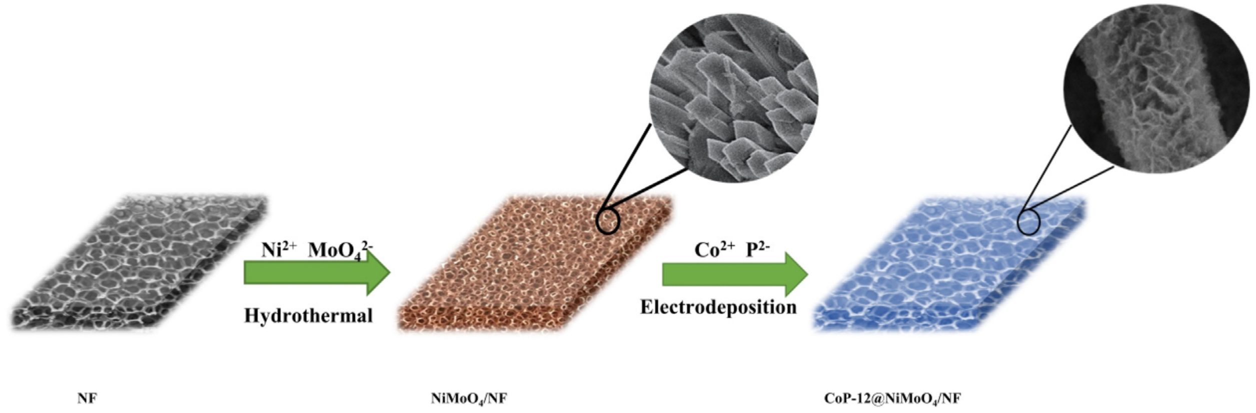

Scheme 1 Schematic illustration for the preparation of the self-supported core-shell structure amorphous CoP-12@$NiMoO_4$/NF electrode.

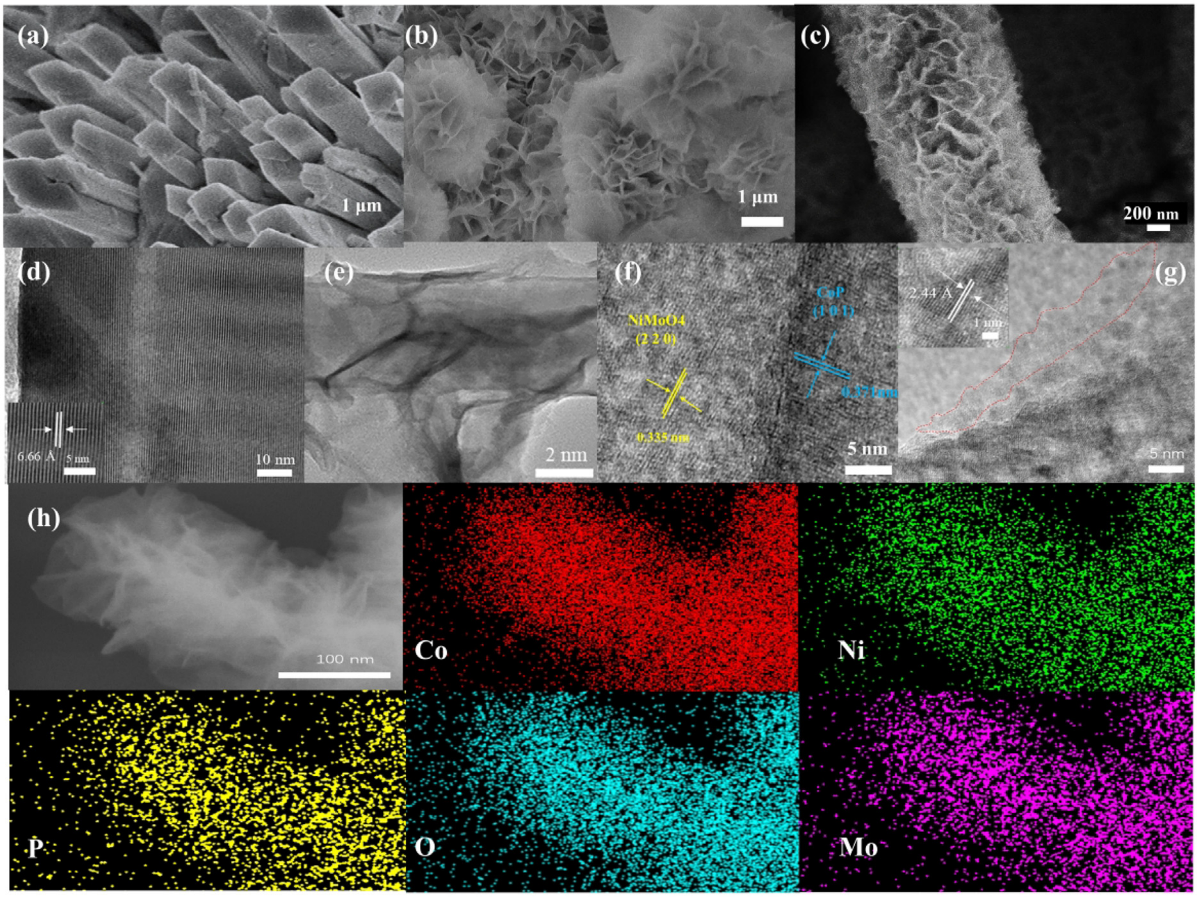

Fig. 1 SEM images of $NiMoO_4$/NF (a), CoP-12/NF (b), CoP-12@$NiMoO_4$/NF (c). HRTEM image of $NiMoO_4$/NF (d). TEM image of CoP-12@$NiMoO_4$/NF (e), HRTEM image of CoP-12@$NiMoO_4$/NF (f), CoP-12 /NF (g). EDS elemental mapping of CoP-12@$NiMoO_4$/NF (h).

13.57° and 29.78° are indexed to (0 0 1), (1 0 0), (0 0 3) planes of $NiMoO_4$ (JCPDS #04–017–0338), respectively. And the typical (2 2 0), which was the intense diffraction peak and (1 3—3) diffraction reflections at $2\theta = 26.59°$ and 48.92°, indicating the formation of β-phase $NiMoO_4$ (PDF#45–0142). All peaks were very consistent with standard diffraction cards and partly with Li (Yang et al., 2021). It was necessary to point out the prepared $NiMoO_4$ (PDF#45–0142) was metastable β-phase (Haetge et al., 2012), which showed higher OER reactivity than stable α-NiMoO4 (Ratha et al., 2017). It was reported that the coordination state of Mo cation caused the distinction of structure between β-$NiMoO_4$ and α-$NiMoO_4$. In α-$NiMoO_4$, the pseudo-octahedral symmetry is formed, which is attributed to the Mo ions coordinate with oxygen atoms. While in β-$NiMoO_4$, the Mo ions are coordinated with oxygen atoms in a distorted tetrahedral state (Kaddouri et al., 2004). Therefore, the prepared $NiMoO_4$ exists in α-$NiMoO_4$ and β-$NiMoO_4$ phase, which are also consistent with the lattice distances in HRTEM images of Fig. 1d and Fig. S2a. The presence of β-$NiMoO_4$ may greatly improve the electrochemical activity of the electrode. Fig. S3 showed that the CoP phase diffraction peak was weak, indicating that the CoP was mainly amorphous phase, which was also corresponding to the HRTEM image in Fig. 1g. The above evidence proved that amorphous CoP nanosheets had been electrodeposited on the surface of $NiMoO_4$ nanorod arrays, which can also be proved in Fig. S4.

The species and chemical valence states of $NiMoO_4$/NF electrode before and after CoP electrodeposition were identified by X-ray photoelectron spectroscopy (XPS), as shown in Fig. S5, Fig. S6 and Fig. 2b-h. The spectra of all the detected elements were corrected by adventitious carbon which is at 284.80 eV (Zhang et al., 2016). It can be found from Fig. S5, there existed Ni, Mo and O elements in $NiMoO_4$/NF electrode, and the high resolution Ni 2p XPS spectra and Mo 3d XPS spectra were shown in Fig. S5b and Fig. S5c. After reasonable CoP electrodeposition, the presence of Co and P elements were appeared in CoP-12@$NiMoO_4$/NF electrode, which were well correlated with EDX mapping. In the CoP-12@$NiMoO_4$/NF electrode, the composition of Ni: Mo: O: Co: P: C was 1.88%: 1.53%: 51.85%: 20.03%: 5.97%: 18.74%. Fig. 2b showed the high resolution O 1 s XPS spectra for CoP-12@$NiMoO_4$/NF, which could be deconvolved into three peaks named as O1, O2 and O3. The O1 peak at 530.20 eV was attributed to the metal–oxygen (M—O) bond, the O2 peak at 531.12 eV was related to the oxygen atoms of hydroxyl group while the O3 peak at 532.41 eV was assigned to the adsorbed water near the surface. Fig. 2c showed the high resolution Ni 2p XPS spectra of CoP-12@$NiMoO_4$/NF electrode, the two peaks at 874.04 eV and 855.92 eV were attributed to Ni

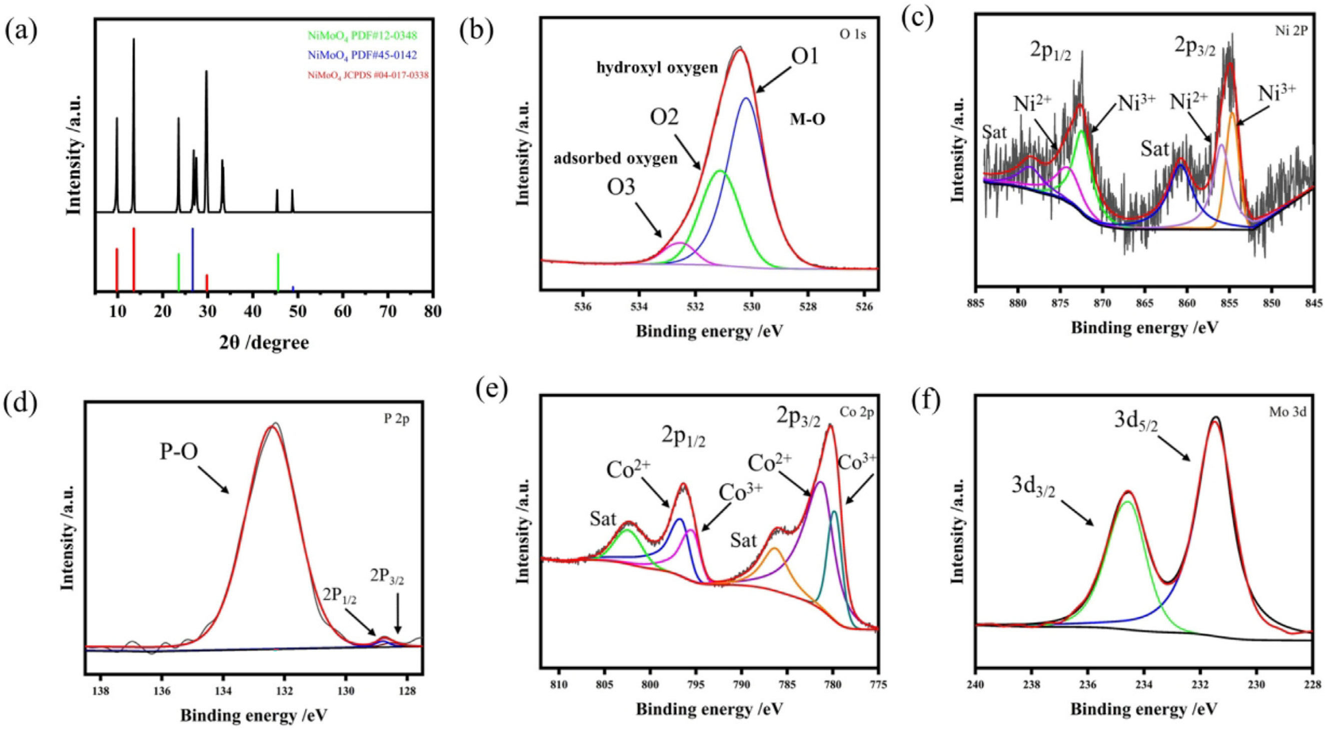

Fig. 2 XRD patterns of $NiMoO_4$ (a). High-resolution XPS spectra for CoP-12@$NiMoO_4$/NF of O 1 s (b), Ni 2p (c), P 2p (d), Co 2p (e), Mo 3d (f).

2p $_{1/2}$ and Ni 2p $_{3/2}$ of Ni $^{2+}$, which were with a separation of 18.12 eV (Zhao et al., 2019). While peaks located at 872.38 eV and 854.66 eV were assigned to Ni 2p $_{1/2}$ and Ni 2p $_{3/2}$ of Ni $^{3+}$. According to the integral areas and the p spin–orbit splitting was 17.8 eV, it can be concluded that the Ni element in prepared catalyst was mainly in the Ni $^{2+}$ state. The atom ratio of Ni^{2+} state and Ni^{3+} state was about 85%:15% (Table S1). A little of Ni^{3+} was probably partially oxidized in the air. As shown in Fig. 2d, the peaks of 128.40 eV and 128.80 eV were attributed to P 2p $_{3/2}$ and P 2p $_{1/2}$. Another peak at 132.42 eV was attributed to the oxidation of the surface resulting from the exposure to air, which caused the oxidation of P element. In the Fig. 2e, the two peaks at 796.64 eV and 781.14 eV were attributed to Co 2p $_{1/2}$ and Co 2p $_{3/2}$ of Co $^{2+}$, respectively. The peaks at 795.40 eV and 779.75 eV were assigned to Co 2p $_{1/2}$ and Co 2p $_{3/2}$ of Co^{3+}, the other two peaks at 802.41 eV and 786.31 eV were related satellite peaks. On the basis of the d-zone theory, transition metals with high d-zone centers can intensify the adsorption capacity of oxygen-containing intermediates, which contribute to enhancing OER performance (Bo et al., 2020). It was obviously that Ni and Co were both mainly in the $Ni^{2+}$and Co^{2+} state. The coexistence of Co^{2+} and Co^{3+} led to abundant oxygen vacancy defects, which played a facilitating role during OER. Fig. 2f showed the high resolution Mo 3d XPS spectra, the peaks of 234.54 eV and 231.40 eV were attributed to Mo 3d $_{3/2}$ and Mo 3d $_{5/2}$, respectively. Since peak positions and the separation were 3.14 eV, according to the d spin–orbit splitting of 3.1 eV, one can find that the presence of Mo^{6+} in the prepared electrode (Chen et al., 2020). The XPS measurement analysis demonstrated that the states of Ni, Mo and O were + 2, + 6 and – 2, respectively, which was consistent well with the chemical formula $NiMoO_4$. The results showed that after electrodeposition, the electron cloud density around the Mo atom decreased due to the existence of core-shell structure, which was evidenced by the small movement toward higher binding energy (from 234.45 to 234.55 eV). It was noteworthy that the binding energy of Ni atoms in CoP-12@$NiMoO_4$ shifted to the right compared with that of $NiMoO_4$. It was well known that P atoms were more electronegative than Ni atoms, but with the formation of heterojunctions, the electron density around Ni atoms still increased, leading to the decrease of BE. As proved by the theoretical analysis below, the formation of CoP-$NiMoO_4$ heterojunctions promoted electron redistribution and optimized the electronic structure. The strong electronic interaction between CoP and $NiMoO_4$ was conducive to regulating the adsorption capacity of the electrode for oxygen-containing intermediates, thereby improving the conductivity and catalytic ability (Sha et al., 2020).

3.2. Electrochemical performance

A standard three-electrode system was used to evaluate the electrocatalysts performance of OER in an alkaline solution (1 M KOH). Fig. 3a showed the LSV curves of the prepared samples. The overpotentials at 10 mA cm^{-2} of NF, $NiMoO_4$/NF, CoP-12/NF, CoP-12@$NiMoO_4$/NF were 320 mV, 217 mV, 307 mV, 165 mV, respectively. The comparison of OER activity of CoP-12@$NiMoO_4$/NF with other reported OER electrocatalysts is shown in Table S2. Obviously, the prepared CoP-12@$NiMoO_4$/NF electrode had excellent electrochemical activity, which is because that CoP-$NiMoO_4$ heterojunctions promotes strong electronic interaction at the interface. In addition, the self-supported core-shell structure

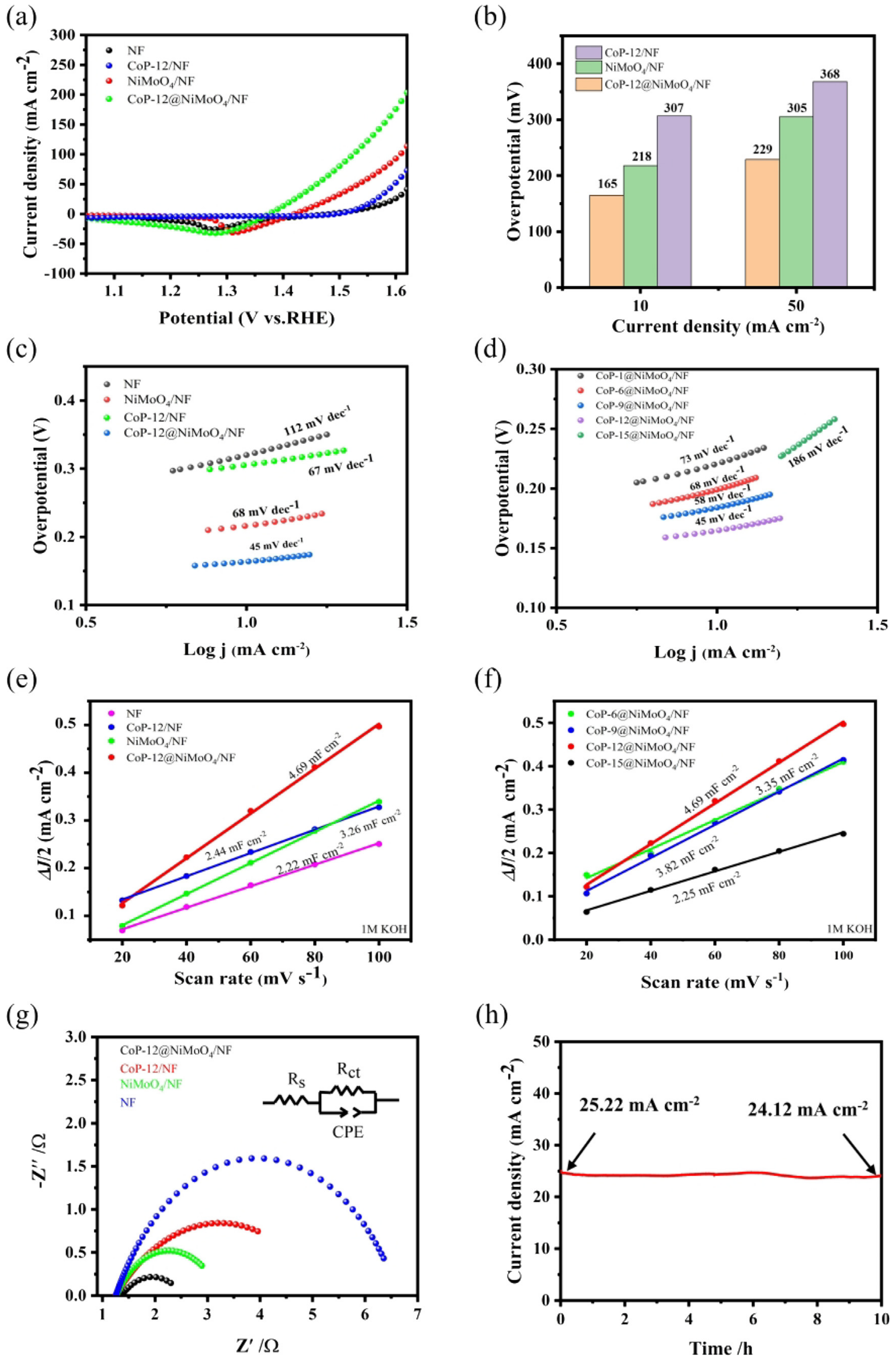

Fig. 3 The LSV curves of prepared electrodes (a). Comparison of overpotentials at 10 and 50 mA cm^{-2} (b). The Tafel slopes of various electrodes (c-d). Linear fitting of double-layer capacitance for different materials (e-f). Nyquist plots of the CoP-12/NF, NiMoO$_4$/NF and CoP-12@NiMoO$_4$/NF electrodes (g). I-T curve of CoP-12@NiMoO$_4$/NF for 10 h (h).

can increase specific surface area, minimize agglomeration and the synergies between core-shell components are also beneficial to the faster transfer of electrons to promote OER performance (Bai et al., 2018). The activity was greatly enhanced by the formation of core-shell structure with CoP-$NiMoO_4$ heterojunctions, which proved that our work was feasible and remarkable. The overpotentials of CoP-1@$NiMoO_4$/NF, CoP-6@$NiMoO_4$/NF, CoP-9@$NiMoO_4$/NF, CoP-12@$NiMoO_4$/NF, CoP-15@$NiMoO_4$/NF were 221 mV, 200 mV, 184 mV, 165 mV, 217 mV, respectively as shown in Fig. S7. The current density increases first and then decrease, and the overpotential increases after decreasing. Because long time electrodeposition led to excessive sediments, the large overlap area between the nanosheets resulted in less effective contact area between electrode and electrolyte. At the same time, the thick electrodeposition layer hindered the overflow of oxygen, which strongly reduced the OER activity. Therefore, the core-shell structure CoP-12@$NiMoO_4$/NF with the suitable electrodeposition time had abundant active sites, which were beneficial to the adsorption of OH-and the electron transfer. As the Fig. 3b shown, under the current density of 10 and 50 mA cm^{-2}, the overpotential of CoP-12@$NiMoO_4$/NF is much lower than that of other electrodes, which fully proved the active reaction kinetics of prepared CoP-12@$NiMoO_4$/NF and the feasibility of this work (Table S3).

Usually, the smaller Tafel slope is associated with the smaller increase of overpotential during OER. As the Fig. 3c shown, the Tafel slopes of NF, CoP-12/NF, $NiMoO_4$/NF, CoP-12@$NiMoO_4$/NF were 112 mV dec^{-1}, 67 mV dec^{-1}, 68 mV dec^{-1} and 45 mV dec^{-1}. It had been proved that the prepared CoP-12@$NiMoO_4$/NF electrode had the most rapid reaction kinetics. In Fig. 3d, the Tafel slopes of CoP-1@$NiMoO_4$/NF, CoP-6@$NiMoO_4$/NF, CoP-9@$NiMoO_4$/NF were 73 mV dec^{-1}, 68 mV dec^{-1}, 58 mV dec^{-1}. However, the Tafel slope of CoP-15@$NiMoO_4$/NF reached 186 mV dec^{-1}. The change trend of the Tafel slope was completely consistent with that of LSV curves. The increase of the Tafel slope was due to the decrease of active sites and the electron transfer channel. Too long electrodeposition time would cause thicker sediments, which impeded electron transfer and decline the reaction kinetics.

Fig. S8 was the CV curves of CoP-12@$NiMoO_4$/NF with the scanning rate from 20 to 100 mV s^{-1} in the no Faradaic interval, which was used as the double-layer capacitance (C_{dl}) to evaluate the electrochemical active surface area (ECSA) during OER (Hu et al., 2019). The CV curves of other prepared electrodes were in the Fig. S9. As shown in Fig. 3e, the double-layer capacitance (C_{dl}) values were 2.22 mF cm^{-2} for NF, 2.44 mF cm^{-2} for CoP-12/NF, 3.26 mF cm^{-2} for $NiMoO_4$/NF and 4.69 mF cm^{-2} for CoP-12@$NiMoO_4$/NF. Therefore, according to the correlation between ECSA and electrochemical OER performance, it can be inferred that CoP-12@$NiMoO_4$/NF had exposed more active sites than the single component sample, which could be due to the the hierarchical core-shell morphology, also facilitating more efficient adsorption of hydroxyl ions. In Fig. 3f, the C_{dl} values of CoP-6@$NiMoO_4$/NF, CoP-9@$NiMoO_4$/NF, CoP-12@$NiMoO_4$/NF, CoP-15@$NiMoO_4$/NF were 3.35 mF cm^{-2}, 3.82 mF cm^{-2}, 4.69 mF cm^{-2}, 2.25 mF cm^{-2}. Obviously, overmuch sediments led to a decrease in ECSA value, indicating that a lot of active sites had disappeared, which was mutually supported by overpotentials of LSV curves and Tafel slopes. In addition, we also calculated the roughness factors (RF) of CoP-12@$NiMoO_4$/NF and CoP-12/NF. The RF was 118 and 61, respectively. Obviously, the active surface area of CoP-12@$NiMoO_4$/NF was twice than that of CoP-12/NF, which demonstrated that CoP-12@$NiMoO_4$/NF core-shell structure had the stronger electrocatalytic activity.

Although ECSA was a key factor, it was not the only one to determine electrocatalyst activity. In this case, the charge transfer dynamics in the OER process were explored by recording electrochemical impedance spectroscopy (EIS) of various electrodes. As the Fig. 3g shown, the semicircle diameter of CoP-12@$NiMoO_4$/NF was smallest compared with CoP-12/NF and $NiMoO_4$/NF electrodes, indicating that prepared CoP-12@$NiMoO_4$/NF electrode had complete local electronic structure, the fastest charge transfer rate and the best conductivity during OER (Table S4). The lowest R_{ct} value of CoP-12@$NiMoO_4$/NF electrode was attributed to the enhanced electronic interaction at the heterojunction interface, which was beneficial to shorten the electron transport distance. Therefore, the kinetic barrier of OER process was reduced. The EIS results were consistent with the above data as well.

In the process of electrolysis of water, the bubbles that generated on the electrode surface rapidly nucleate, adsorb, aggregate and separate, which can produce small fluctuations with the change of voltage, thus decreasing the electrocatalytic activities (Hu et al., 2021). Therefore, it was necessary to test the stability of the electrocatalyst. After 5000 cycles CV, the overpotential of prepared CoP-12@$NiMoO_4$/NF electrode changed from 165 mV to 181 mV (Fig. S10), indicating that the electrode had little electrochemical activity degradation after 5000 cycles CV. In order to further explore the stability, CoP-12@$NiMoO_4$/NF electrode was also tested by chronoamperometry at a fixed potential in 1 M KOH. As the Fig. 3h and Fig. S11 shown, CoP-12@$NiMoO_4$/NF electrode showed steady durability under a certain voltage for 10 h long-term electrochemical process with negligible degradation and the good stability of different current densities. The excellent performance of CoP-12@$NiMoO_4$/NF electrode was attributed to the good growth of CoP nanosheets on $NiMoO_4$ nanorod arrays to form a core-shell structure under the appropriate conditions. The core-shell structure facilitated the adsorption of reactants, intermediate transformation and the product desorption, which avoided the material agglomerate and promoted the rapid release of O_2 in close contact with the electrolyte. In the Fig. 3h, the small current attenuation may be attributed to sectional oxidation of CoP during OER (Jin, 2017). It had been shown that although metal phosphates were easily oxidized during OER, they still had more electrochemical activity than the corresponding hydroxide or oxide, possibly because OER process could produce more catalytic active sites, making it promising for practical applications (Xu et al., 2018). And in Fig. S12, the high OER Faradic efficiency for CoP-12@$NiMoO_4$ has shown that it can achieve efficient catalysis while maintaining long-term stability. The morphology of CoP-12@$NiMoO_4$/NF before and after 5000 cycles CV was compared to research structural stability. As shown in Fig. S13, the structure of CoP nanosheets was still relatively complete, indicating the electrode had a good structural stability. The outstanding structure stability of CoP-12@$NiMoO_4$/NF was mainly attributed to the direct growth of the active material on NF without the polymer binder and additional conductive additives, which reduced the undesirable interface of the electrode and maintained the structure under high current density.

XPS technology was used to investigate the chemical composition and the oxidative state change of CoP-12@$NiMoO_4$/NF electrode before and after 5000 CV cycles in 1 M KOH. The image in Fig. 4a showed that Ni, Mo O, Co and P elements still existed but the intensity of Mo peak and P peak decreased significantly. In the high resolution O 1 s XPS spectra of Fig. 4b, there were three peaks appeared at 530.00 eV, 531.12 eV and 528.20 eV. Obviously, the M−O bond and the oxygen atoms of hydroxyl groups still existed, the peak at 532.41 eV of the adsorbed water on the surface disappeared. But there was a new peak at 528.20 eV, which was attributed to the new hydroxyl species. In the high resolution Ni 2p XPS spectra of Fig. 4c, the two peaks at 873.72 eV and 855.77 eV were assigned to Ni 2p $_{1/2}$ and Ni 2p $_{3/2}$ of Ni $^{2+}$, respectively. While peaks located at 871.83 eV and 854.31 eV were assigned to Ni 2p $_{1/2}$ and Ni 2p $_{3/2}$ of Ni $^{3+}$. As Fig. 4d shown, the peak at 127.55 eV was assigned to P 2p $_{3/2}$, the other peak at 131.79 eV was assigned into P-O bond. In Fig. 4e, the two peaks at 795.14 eV and 780.94 eV were attributed to Co 2p $_{1/2}$ and Co 2p $_{3/2}$ of Co $^{2+}$, respectively. The peaks at 793.94 eV and 778.83 eV were assigned to Co 2p $_{1/2}$ and Co 2p $_{3/2}$ of Co^{3+}. In the high resolution Mo 3d XPS spectra of Fig. 4f, the peaks of 234.01 eV and 230.92 eV were attributed to Mo 3d $_{3/2}$ and Mo 3d $_{5/2}$, respectively. And the peak at 227.30 eV was assigned to Mo^{5+}. It showed that Mo had more metallic properties. After 5000 cycles CV, the composition of Ni: Mo: O: Co: P: C was 9.49%: 0.52%: 41.97%: 7.28%: 1.36%: 39.39%. It can be simply found that the content of Ni increased significantly, while the content of Mo decreased greatly. Mo was dissolved or leach out, maybe resulting in the formation of nickel hydroxide. At the same time, the bond shape also demonstrated a large increase in nickel hydroxide. And the atom ratio of Ni^{2+} state and Ni^{3+} state was changed from 85%: 15% to 40%: 60% (Table S1). The Co 2p related peaks also shifted slightly towards lower BE, but the band shape was the same as that before 5000 cycles CV, thus confirming the presence and excellent stability of the CoP compound. Meanwhile a little Co species were converted to a higher oxidation state of Co^{3+}. Particularly, the rapid decay of Co-P bond signal had also indicated that the phosphide had been oxidized to form a hydroxyl oxide. The increase of the valence was conducive to the combination with oxygen-containing species in the reaction, which had produced more active sites and enhanced the OER performance (Lv et al., 2020; Feng et al., 2020). Since the anodic potential further oxidized the metals on the catalyst surface, an increase in the oxidation state should have been observed. However, for our experiment, after 5000 cycles CV, the BE of Mo, Ni, and Co atoms all shifted to a lower value. Therefore, it is reasonable to infer that the metal cations (Ni, Co, and Mo) participate in the interface electron transfer process in the OER process. It was also proved that the heterojunction which was formed at the interface promoted the electron transfer, optimized the local electron structure and enhanced the OER performance.

3.3. Theoretical investigation

To investigate the reason for OER activity of CoP-12@$NiMoO_4$/NF, precise DFT calculations were studied based on the HRTEM, XPS, XRD and theoretical calculations results comprehensively. The details of the calculations were described in the "Supporting Information". The configura-

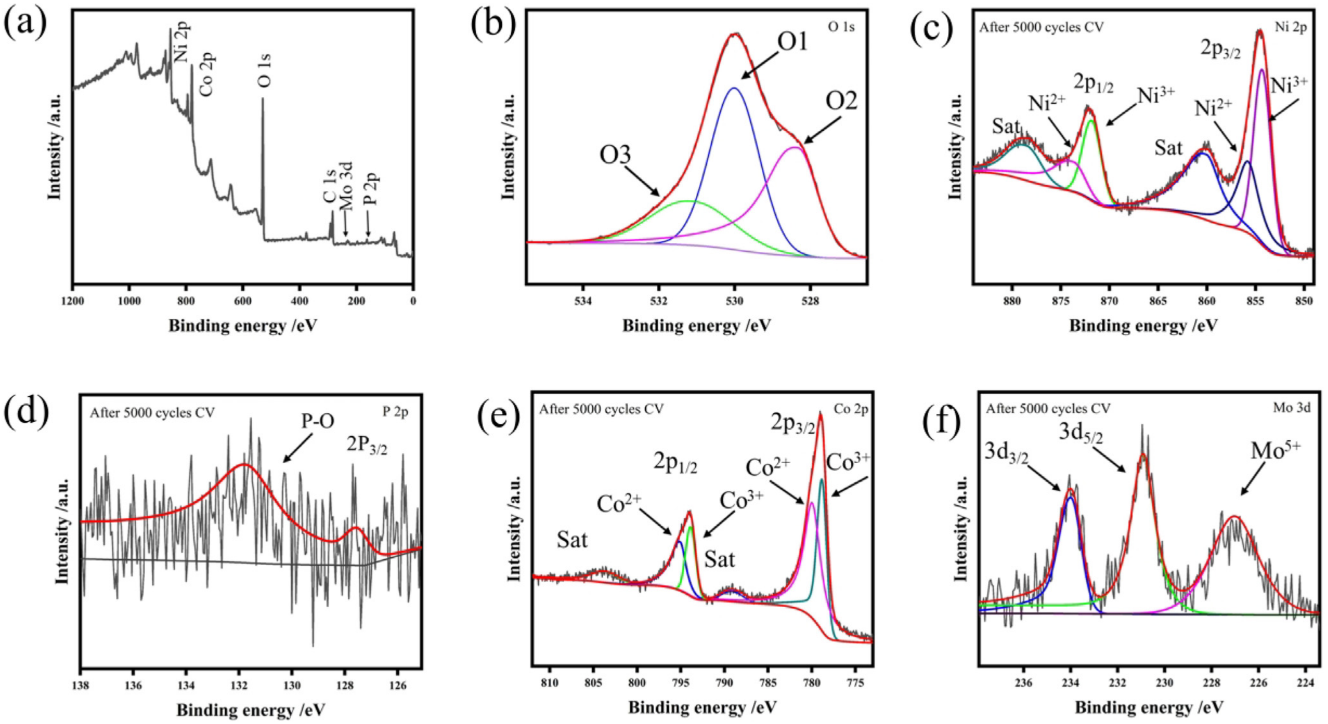

Fig. 4 XPS survey spectrum of CoP-12@$NiMoO_4$/NF after 5000 CV cycles (a). High-resolution XPS spectra after 5000 CV cycles of O 1 s (b), Ni 2p (c), P 2p (d), Co 2p (e), Mo 3d (f).

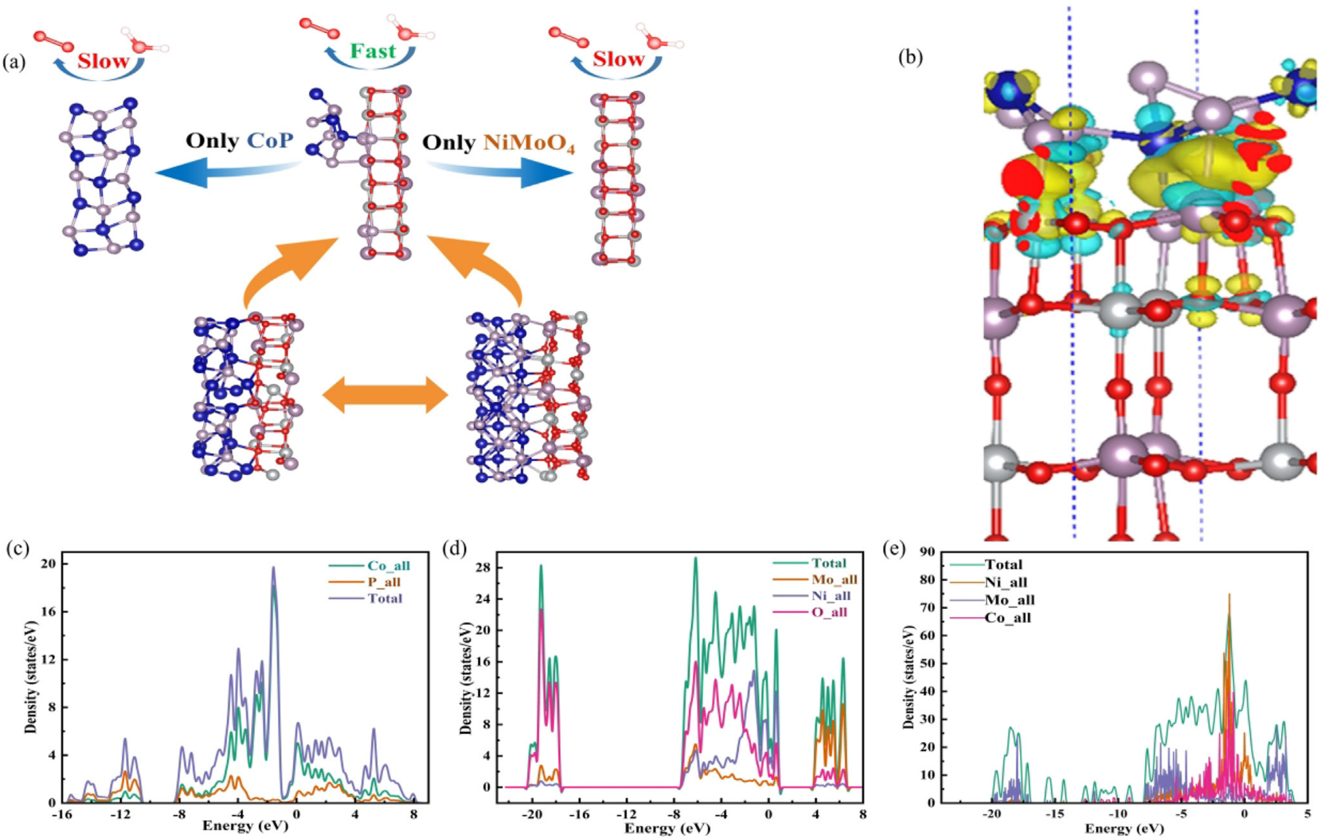

Fig. 5 Schematic image of OER (a). The differential charge density image of CoP-12@$NiMoO_4$/NF (b). The image of the density of states for CoP (c), $NiMoO_4$ (d) and CoP-12@$NiMoO_4$/NF (e).

tional structure of CoP, $NiMoO_4$, and CoP-$NiMoO_4$ heterojunction were displayed in Fig. 5a. As shown in Fig. 5b, the differential charge density indicated that the heterojunction surfaces exhibited differential electron distribution. Yellow and cyan represented the accumulation and depletion of charge in space respectively, which evidently demonstrated the charge transfer on the boundary area from $NiMoO_4$ to CoP. Such a heterojunction can disrupt the periodicity of the surface by introducing an amorphous CoP structure, resulting in an uneven charge distribution around the CoP, which was consistent with the XPS analysis, proving the strong electronic interactions of CoP-$NiMoO_4$ heterojunction. In order to gain insight into the electron transfer at the CoP-$NiMoO_4$ heterojunction interface, the density of states was subsequently supplemented in Fig. 5c-e. The density of states for CoP from about 0 to -4 eV was highest, which was consisted with the energy band diagram in Fig. 6a. And the density for $NiMoO_4$ from about -8 to -18 eV was zero, which exhibited poor electrical conductivity as Fig. 6b shown. Compared with both of them, CoP-12@$NiMoO_4$/NF electrode displayed a smallest bandgap showing the improved conductivity. Furthermore, when CoP-$NiMoO_4$ heterojunction was formed, more Co elements entered the forbidden band, therefore, the electrons redistributed at the interface, where it can be seen that the CoP-$NiMoO_4$ (75 eV) heterojunction interface had higher DOS near the Fermi level than the single component sample of CoP (20 eV) and $NiMoO_4$ (28 eV), indicating that the electronic structure of CoP-$NiMoO_4$ heterojunction and the metallic properties were conducive to rapid electron transfer in OER, which can be supported by the smallest R_{ct} of CoP-12@$NiMoO_4$/NF electrode.

OER free energy for CoP, $NiMoO_4$ and CoP-$NiMoO_4$ heterojunction was calculated at Co sites. The reaction energy barrier was an important parameter for evaluating catalytic activity, which can be considered as the free energy of the rate-determining step (RDS) (Xing et al., 2022). As shown in Fig. 6c-d, the RDS at 0 V of CoP and $NiMoO_4$ was the fourth step of the OOH* decomposition reaction, which the reaction energy barrier was 8.743 eV and 7.685 eV, respectively. OOH* should have been more active than the intermediates of O* and OH*, but the reasons for this situation can attribute to the stable six-member ring structure of *OOH, which was forming hydrogen bonds with the exposed oxygen atoms on the surface of $NiMoO_4$. In the Fig. 6e-f, the exciting thing was that not only the RDS at 0 V for CoP-$NiMoO_4$ heterojunction was changed to the first step, but also the reaction energy barrier of RDS was reduced to only 2.519 eV, which was down to about 1/4 compared with CoP. And the RDS of CoP, $NiMoO_4$ and CoP-$NiMoO_4$ heterojunction were not changed at 1.23 V, however, extra voltage had reduced the reaction energy barrier of RDS. In addition, combined with the difference of electrostatic potential of CoP, $NiMoO_4$ and CoP-$NiMoO_4$ heterojunction in Fig. S14-15, it can be clearly concluded that the formation of CoP-$NiMoO_4$ heterojunction can increase electrostatic potential. And the high electrostatic potential was conducive to OER reaction.

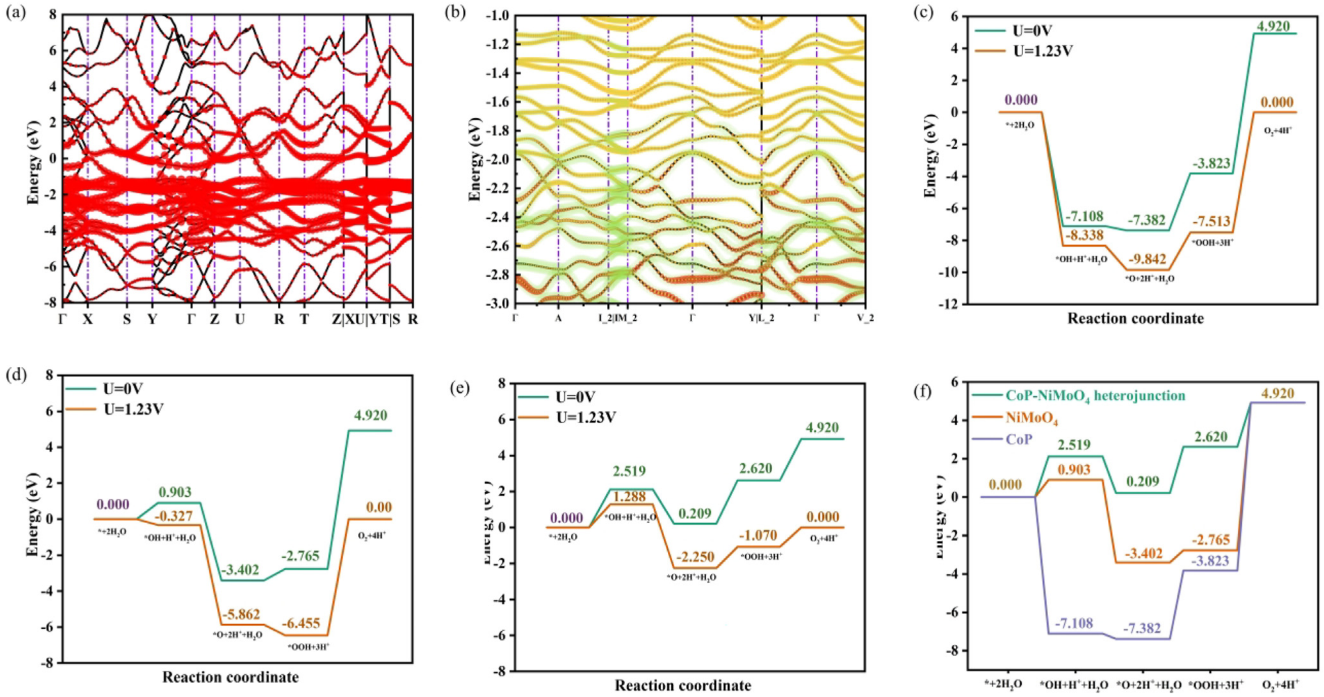

Fig. 6 Band diagram and element projection of CoP (red is Co, black is P) (a) and $NiMoO_4$ (red is Mo, yellow is Ni and purple is O) (b). Free energy diagram of OER intermediates for CoP (c), $NiMoO_4$ (d) and CoP-$NiMoO_4$ (e). Free energy diagram of OER intermediates at U = 0 V (f).

4. Conclusion

In conclusion, the self-supported CoP-12@$NiMoO_4$/NF electrode with core-shell heterojunction structure had been prepared successfully through a feasible two-step hydrothermal and electrodeposition route. A large number of CoP nanosheets were excellently deposited on the surface of $NiMoO_4$ nanorods arrays, which greatly increased the active sites. The constructed CoP-12@$NiMoO_4$/NF electrode only required a low overpotential of 165 mV in 1 M KOH to achieve a current density of 10 mA cm^{-2}. In addition, the CoP-12@$NiMoO_4$/NF electrode also had the smallest Tafel slope (44 mV dec^{-1}), largest ECSA (4.69 mF cm^{-2}) and lowest charge transfer resistance (1.207 Ω) among this series samples. Especially, the CoP-12@$NiMoO_4$/NF electrode had an outstanding cyclic stability and long-term stability. DFT calculations indicated that CoP-12@$NiMoO_4$/NF electrode can reduce reaction energy barrier of RDS from 8.743 eV to 2.519 eV, showing rapid reaction kinetics, and enhancing OER activity. Obviously, this work was a ponderable attempt to construct a non-noble metal catalyst with excellent OER performance, which had provided a new route in practical application in the future.

CRediT authorship contribution statement

Nu Wang: Validation, Writing – original draft, Formal analysis, Visualization. **Kai Huo:** Visualization. **Hongli Zhu:** Data curation. **Haoran Zi:** Data curation. **Yan Shan:** Data curation, Formal analysis. **Kezheng Chen:** Visualization, Funding acquisition. **Xuegang Yu:** Data curation, Formal analysis.

Declaration of Competing Interest

The authors declare that they have no known competing financial interests or personal relationships that could have appeared to influence the work reported in this paper.

Acknowledgment

The authors gratefully acknowledge financial support by the National Natural Science Foundation of China (Grant No. 51472133), Natural Science Foundation of Shandong Province of China (Grant No. ZR2020ME049), Teaching Reform Research Project of Shandong Province of China (Grant No. Z2021041).

Appendix A. Supplementary material

Supplementary data to this article can be found online at https://doi.org/10.1016/j.arabjc.2023.105157.

References

Bai, J., Meng, T.M., Guo, D.L., Wang, S.G., Mao, B.G., Cao, M.H., 2018. Co_9S_8@MoS_2 core shell heterostructures as trifunctional electrocatalysts for overall water splitting and Zn air batteries. ACS Appl. Mater. Interfaces 10, 1678–1689.

Bhanja, P., Kim, Y., Paul, B., Lin, J.J., Alshehri, S.M., Ahamad, T., Kaneti, Y.V., Bhaumik, A., Yamauchi, Y., 2020. Facile synthesis of nanoporous transition metal-based phosphates for oxygen evolution reaction. ChemCatChem 12, 2091–2096.

Bo, X., Hocking, R.K., Zhou, S., Li, Y.B., Chen, X.J., Zhuang, J.C., Du, Y., Zhao, C., 2020. Capturing the active sites of multimetallic (oxy)hydroxides for the oxygen evolution reaction. Energy Environ. Sci. 13, 4225–4237.

Chen, F.S., Ji, S., Liu, Q.B., Wang, H., Liu, H., Brett, D.J.L., Wang, G.X., Wang, R.F., 2018. Rational design of hierarchically core-shell structured Ni_3S_2@$NiMoO_4$ nanowires for electrochemical energy storage. Small 14, 8.

Chen, L., Xu, G.C., Xu, G., Zhang, L., Ding, H., 2020. Co-based coordination polymer-derived Co_3S_4 nanotube decorated with

$NiMoO_4$ nanosheets for effective oxygen evolution reaction. Int. J. Hydrogen Energy 45, 30463–30472.

Chen, L., Ren, W.Q., Xu, C.X., Chen, Q., Chen, Y.Y., Wang, W., Xu, W.Y., Hou, Z.H., 2022. Oxygen vacancy assisted low-temperature synthesis of P-doped Co_3O_4 with enhanced activity towards oxygen evolution reaction. J. Alloys Compd. 894, 8.

Chu, S., Majumdar, A., 2012. Opportunities and challenges for a sustainable energy future. Nature 488, 294–303.

Dastafkan, K., Li, Y.B., Zeng, Y.C., Han, L., Zhao, C., 2019. Enhanced surface wettability and innate activity of an iron borate catalyst for efficient oxygen evolution and gas bubble detachment. J. Mater. Chem. A 7, 15252–15261.

Dutta, A., Samantara, A.K., Dutta, S.K., Jena, B.K., Pradhan, N., 2016. Surface-oxidized dicobalt phosphide nanoneedles as a non-precious, durable, and efficient OER catalyst. ACS Energy Lett. 1, 169–174.

Feng, D.Y., Dong, Y.B., Zhang, L.L., Ge, X., Zhang, W., Dai, S., Qiao, Z.A., 2020. Holey lamellar high-entropy oxide as an ultra-high-activity heterogeneous catalyst for solvent-free aerobic oxidation of benzyl alcohol. Angew. Chem.-Int. Edit. 59, 19503–19509.

Ghosh, S., Basu, R.N., 2018. Multifunctional nanostructured electrocatalysts for energy conversion and storage: current status and perspectives. Nanoscale 10, 11241–11280.

Guo, R.H., Lai, X.X., Huang, J.W., Du, X.C., Yan, Y.C., Sun, Y.H., Zou, G.F., Xiong, J., 2018. Phosphate-based electrocatalysts for water splitting: Recent progress. ChemElectroChem 5, 3822–3834.

Haetge, J., Djerdj, I., Brezesinski, T., 2012. Nanocrystalline $NiMoO_4$ with an ordered mesoporous morphology as potential material for rechargeable thin film lithium batteries. Chem. Commun. 48, 6726–6728.

Hu, X.J., Li, T.C., Tang, Y.D., Wang, Y.R., Wang, A., Fu, G.T., Li, X.D., Tang, Y.W., 2019. Hydrogel-derived honeycomb Ni_3S_4/N, P-C as an efficient oxygen evolution catalyst. Chem.-Eur. J. 25, 7561–7568.

Hu, Q., Wang, Z.Y., Huang, X.W., Qin, Y.J., Yang, H.P., Ren, X.Z., Zhang, Q.L., Liu, J.H., Shao, M.H., He, C.X., 2021. Integrating well-controlled core-shell structures into "superaerophobic" electrodes for water oxidation at large current densities. Appl. Catal. B-Environ. 286, 8.

Jin, S., 2017. Are metal chalcogenides, nitrides, and phosphides oxygen evolution catalysts or bifunctional catalysts? ACS Energy Lett. 2, 1937–1938.

Jin, H.Y., Wang, X.S., Tang, C., Vasileff, A., Li, L.Q., Slattery, A., Qiao, S.Z., 2021. Stable and highly efficient hydrogen evolution from seawater enabled by an unsaturated nickel surface nitride. Adv. Mater. 33, 8.

Kaddouri, A., Tempesti, E., Mazzocchia, C., 2004. Comparative study of beta-nickel molybdate phase obtained by conventional precipitation and the sol-gel method. Mater. Res. Bull. 39, 695–706.

Kim, B.K., Kim, S.K., Cho, S.K., Kim, J.J., 2018. Enhanced catalytic activity of electrodeposited Ni-Cu-P toward oxygen evolution reaction. Appl. Catal. B-Environ. 237, 409–415.

Li, N., Hu, Z., Li, M., Zhang, L.H., Hu, S., 2020. Self-assembly of NiFe-LDH with birnessite via electrostatic attraction towards high-performance OER catalyst. Mater. Lett. 281, 4.

Li, M.X., Liu, Z.H., Zha, Q.Q., Li, S.F., Ni, Y.H., 2021. Non-precious metal nanotube arrays hybrid catalyst prepared by a mutual template method for efficient water oxidation in alkaline medium. Chem. Eng. J. 410, 9.

Liu, G., Wang, M.H., Wu, Y., Li, N., Zhao, F., Zhao, Q., Li, J.P., 2020. 3D porous network heterostructure NiCe@NiFe electrocatalyst for efficient oxygen evolution reaction at large current densities. Appl. Catal. B-Environ. 260, 8.

Lv, X.D., Li, X.T., Yang, C., Ding, X.Q., Zhang, Y.F., Zheng, Y.Z., Li, S.Q., Sun, X.N., Tao, X., 2020. Large-size, porous, ultrathin NiCoP nanosheets for efficient electro/photocatalytic water splitting. Adv. Funct. Mater. 30, 10.

Ma, M., Zhu, G.L., Xie, F.Y., Qu, F.L., Liu, Z., Du, G., Asiri, A.M., Yao, Y.D., Sun, X.P., 2017. Homologous catalysts based on Fe-doped CoP nanoarrays for high-performance full water splitting under benign conditions. ChemSusChem 10, 3188–3192.

Ratha, S., Samantara, A.K., Singha, K.K., Gangan, A.S., Chakraborty, B., Jena, B.K., Rout, C.S., 2017. Urea-assisted room temperature stabilized metastable beta-NiMoO4: Experimental and theoretical insights into its unique bifunctional activity toward oxygen evolution and supercapacitor. ACS Appl. Mater. Interfaces 9, 9640–9653.

Sha, L.N., Liu, T.F., Ye, K., Zhu, K., Yan, J., Yin, J.L., Wang, G.L., Cao, D.X., 2020. A heterogeneous interface on NiS@Ni_3S_2/$NiMoO_4$ heterostructures for efficient urea electrolysis. J. Mater. Chem. A 8, 18055–18063.

Shen, X.R., Li, H.J., Zhang, Y.Y., Ma, T.T., Li, Q., Jiao, Q.Z., Zhao, Y., Li, H.S., Feng, C.H., 2022. Construction dual-regulated $NiCo_2S_4$@Mo-doped CoFe-LDH for oxygen evolution reaction at large current density. Appl. Catal. B-Environ. 319, 10.

Turner, J.A., 2004. Sustainable hydrogen production. Science 305, 972–974.

Wang, B.Q., Han, X., Guo, C., Jing, J., Yang, C., Li, Y.P., Han, A.J., Wang, D.S., Liu, J.F., 2021. Structure inheritance strategy from MOF to edge-enriched NiFe-LDH array for enhanced oxygen evolution reaction. Appl. Catal. B-Environ. 298, 7.

Wang, C., Shang, H.Y., Li, J., Wang, Y., Xu, H., Wang, C.Y., Guo, J., Du, Y.K., 2021. Ultralow Ru doping induced interface engineering in MOF derived ruthenium-cobalt oxide hollow nanobox for efficient water oxidation electrocatalysis. Chem. Eng. J. 420, 8.

Wang, Y., Sun, Y., Yan, F., Zhu, C.L., Gao, P., Zhang, X.T., Chen, Y.J., 2018. Self-supported NiMo-based nanowire arrays as bifunctional electrocatalysts for full water splitting. J. Mater. Chem. A 6, 8479–8487.

Wu, L.B., Yu, L., Zhang, F.H., McElhenny, B., Luo, D., Karim, A., Chen, S., Ren, Z.F., 2021. Heterogeneous bimetallic phosphide Ni_2P-Fe_2P as an efficient bifunctional catalyst for water/seawater splitting. Adv. Funct. Mater. 31, 12.

Wu, L.B., Zhang, F.H., Song, S.W., Ning, M.H., Zhu, Q., Zhou, J.Q., Gao, G.H., Chen, Z.Y., Zhou, Q.C., Xing, X.X., Tong, T., Yao, Y., Bao, J.M., Yu, L., Chen, S., Ren, Z.F., 2022. Efficient alkaline water/seawater hydrogen evolution by a nanorod-nanoparticle-structured Ni-MoN catalyst with fast water-dissociation kinetics. Adv. Mater. 34, 12.

Xiao, P., Chen, W., Wang, X., 2015. A review of phosphide-based materials for electrocatalytic hydrogen evolution. Adv. Energy Mater. 5, 13.

Xing, G.Y., Tong, M.M., Yu, P., Wang, L., Zhang, G.Y., Tian, C.G., Fu, H.G., 2022. Reconstruction of highly dense Cu-N_4 active sites in electrocatalytic oxygen reduction characterized by operando synchrotron radiation. Angew. Chem.-Int. Edit. 61, 10.

Xu, J.Y., Li, J.J., Xiong, D.H., Zhang, B.S., Liu, Y.F., Wu, K.H., Amorim, I., Li, W., Liu, L.F., 2018. Trends in activity for the oxygen evolution reaction on transition metal (M = Fe Co, Ni) phosphide precatalysts. Chem. Sci. 9, 3470–3476.

Yan, H.J., Tian, C.G., Wang, L., Wu, A.P., Meng, M.C., Zhao, L., Fu, H.G., 2015. Phosphorus-modified tungsten nitride/reduced graphene oxide as a high-performance, non-noble-metal electrocatalyst for the hydrogen evolution reaction. Angew. Chem.-Int. Edit. 54, 6325–6329.

Yan, J.M., Zhang, X.B., Akita, T., Haruta, M., Xu, Q., 2010. One-step seeding growth of magnetically recyclable Au@Co core-shell nanoparticles: Highly efficient catalyst for hydrolytic dehydrogenation of ammonia borane. J. Am. Chem. Soc. 132, 5326-+.

Yang, F.N., Luo, Y.T., Yu, Q.M., Zhang, Z.Y., Zhang, S., Liu, Z.B., Ren, W.C., Cheng, H.M., Li, J., Liu, B.L., 2021. A durable and efficient electrocatalyst for saline water splitting with current density exceeding 2000 mA cm^{-2}. Adv. Funct. Mater. 31, 10.

Yang, R., Zhou, Y.M., Xing, Y.Y., Li, D., Jiang, D.L., Chen, M., Shi, W.D., Yuan, S.Q., 2019. Synergistic coupling of CoFe-LDH arrays with NiFe-LDH nanosheet for highly efficient overall water splitting in alkaline media. Appl. Catal. B-Environ. 253, 131–139.

Yoon, T., Kim, K.S., 2016. One-step synthesis of CoS-doped beta-Co $(OH)_2$@Amorphous MoS_{2+x} hybrid catalyst grown on nickel foam for high-performance electrochemical overall water splitting. Adv. Funct. Mater. 26, 7386–7393.

Yu, L., Zhou, H.Q., Sun, J.Y., Qin, F., Yu, F., Bao, J.M., Yu, Y., Chen, S., Ren, Z.F., 2017. Cu nanowires shelled with NiFe layered double hydroxide nanosheets as bifunctional electrocatalysts for overall water splitting. Energy Environ. Sci. 10, 1820–1827.

Yu, L., Zhou, H.Q., Sun, J.Y., Mishra, I.K., Luo, D., Yu, F., Yu, Y., Chen, S., Ren, Z.F., 2018. Amorphous NiFe layered double hydroxide nanosheets decorated on 3D nickel phosphide nanoarrays: a hierarchical core-shell electrocatalyst for efficient oxygen evolution. J. Mater. Chem. A 6, 13619–13623.

Yu, L., Zhu, Q., Song, S.W., McElhenny, B., Wang, D.Z., Wu, C.Z., Qin, Z.J., Bao, J.M., Yu, Y., Chen, S., Ren, Z.F., 2019. Non-noble metal-nitride based electrocatalysts for high-performance alkaline seawater electrolysis. Nat. Commun. 10, 10.

Yu, L., Wu, L.B., Song, S.W., McElhenny, B., Zhang, F.H., Chen, S., Ren, Z.F., 2020. Hydrogen generation from seawater electrolysis over a sandwich-like NiCoN|Ni_xP|NiCoN microsheet array catalyst. ACS Energy Lett. 5, 2681–2689.

Zhang, F.H., Liu, Y.F., Wu, L.B., Ning, M.H., Song, S.W., Xiao, X., Hadjiev, V.G., Fan, D.E., Wang, D.Z., Yu, L., Chen, S., Ren, Z.F., 2022. Efficient alkaline seawater oxidation by a three-dimensional core-shell dendritic NiCo@NiFe layered double hydroxide electrode. Mater. Today Phys. 27, 6.

Zhang, X.S., Su, H., Du, X.Q., 2020. A nickel molybdenum oxide nanoarray as an efficient and stable electrocatalyst for overall water splitting. New J. Chem. 44, 8176–8182.

Zhang, J., Wang, T., Liu, P., Liao, Z.Q., Liu, S.H., Zhuang, X.D., Chen, M.W., Zschech, E., Feng, X.L., 2017. Efficient hydrogen production on $MoNi_4$ electrocatalysts with fast water dissociation kinetics. Nat. Commun. 8, 8.

Zhang, B., Xiao, C.H., Xie, S.M., Liang, J., Chen, X., Tang, Y.H., 2016. Iron-nickel nitride nanostructures in situ grown on surface-redox-etching nickel foam: Efficient and ultrasustainable electrocatalysts for overall water splitting. Chem. Mater. 28, 6934–6941.

Zhao, X.Y., Meng, J., Yan, Z.H., Cheng, F.Y., Chen, J., 2019. Nanostructured $NiMoO_4$ as active electrocatalyst for oxygen evolution. Chin. Chem. Lett. 30, 319–323.